Journal of Power Sources 195 (2010) 7930–7942

Contents lists available at ScienceDirect

Journal of Power Sources

journal homepage: www.elsevier.com/locate/jpowsour

Characterization and analysis methods for the examination of the heterogeneous solid oxide fuel cell electrode microstructure. Part 1: Volumetric measurements of the heterogeneous structure

Kyle N. Grew, Aldo A. Peracchio, Abhijit S. Joshi, John R. Izzo Jr., Wilson K.S. Chiu*

Department of Mechanical Engineering, University of Connecticut, 191 Auditorium Rd., Storrs, CT 06269-3139, United States

ARTICLE INFO

Article history:
Received 1 April 2010
Received in revised form 2 July 2010
Accepted 5 July 2010
Available online 11 August 2010

Keywords:
Microstructure
X-ray
Lattice Boltzmann
Transport

ABSTRACT

Advanced imaging and characterization methods have permitted the 3-D and phase-specific reconstruction of dense and opaque samples with features that have a length scale on the order of tens of nanometers and comprised of materials with large X-ray mass absorption coefficients. Engineered materials, like those found in solid oxide fuel cell (SOFC) electrodes, use complex materials that have often limited opportunities to perform 3-D characterization and analysis. Still, characterization and analysis methods are needed to better understand these structures and their functional impact. The development, verification, and validation of methods used by the authors for the characterization and analysis of the heterogeneous SOFC anode are discussed in this work [1,2]. These methods include the measurement of the volume fractions of the individual phases, contiguity or volumetric connectivity, tortuosity, and interfacial properties. A second and complementary part of this work will examine quantitative methods that provide detailed descriptions of the structure and its relations to the transport processes that it must support [3]. These efforts are intended to describe the formulation of methods developed to provide insight into the SOFC anode nano/microstructure.

1. Introduction

A detailed understanding of the microstructure and functional behavior of engineered materials, as related to the environment and conditions it must operate and/or be stored in, are critical to the development of advanced technologies. A recent Department of Energy (DOE) report on basic research needs for electrical energy storage highlights four cross-cutting research needs that are critical to meeting future energy storage needs: (i) advances in characterization, (ii) nanostructured materials, (iii) innovations in electrolytes, and (iv) theory, modeling, and simulation [4]. This report goes on to suggest that the fundamental challenges associated with building a scientific foundation for providing comprehensive descriptions of transport and charge transfer at the interfaces is paramount. This effort requires new analysis tools that are capable of characterizing processes at unprecedented spatial and temporal resolutions. Although this report focuses on direct electrical energy storage often attributed to batteries and capacitors, the concept is the same for energy conversion technologies like the SOFC.

Strategies targeted for these efforts include the examination of structural properties and changes over nanometer to macroscopic length scales, examination of structure and reactivity of relevant interfaces, and the imaging of structural, electrochemical, and physical/electronic properties. Multi-scale modeling and simulation is identified as providing unparalleled opportunities to understand the complexities of these processes [4]. Similar needs have been highlighted in DOE reports on basic research needs for catalysis for energy [5], next generation photon sources [6], and materials under extreme environments [7].

The characterization of the SOFC microstructure can be a key component to the realization of the opportunities afforded by the technology. Thermochemical stability and durability are among the more substantial challenges facing SOFCs. In the SOFC anode, degradation due to Ni coarsening/aging [8–12], redox cycling [10,12–16], thermal expansion and residual strain effects [10,17,18], coking [10,19–22] and sulfur-poisoning [10] from various fuels, and impurities forming at the electrochemical interfaces [23] are widely studied. Characterization can provide the necessary insights regarding the details of the microstructure and how it responds to different manufacturing processes, environments, and operational conditions. The use of computational analysis efforts, which are aimed at gaining insights into the underlying implications of the microstructure on the cell performance and how it changes in conjunction with these efforts,

* Corresponding author. Tel.: +1 860 486 3647; fax: +1 860 486 5088..
E-mail address: wchiu@engr.uconn.edu (W.K.S. Chiu).

0378-7753/$ – see front matter © 2010 Elsevier B.V. All rights reserved.
doi:10.1016/j.jpowsour.2010.07.005

Table 1
Descriptions of the samples that were considered in this analysis [1,2].

Sample ID	Sample location	Phases examined	X-ray source & energy level, keV	Max. voxels considered	Pixel edge length, nm	Resolution, nm
1	Interface	Ni/YSZ/Pore	APS beamline 32-ID 8.317 8.357	150^3	16.2	38.5
2	Interface	Dense/Pore	Laboratory Cu K_α 8.05	150^3	41.7	42.7
3	Support	Dense/Pore	Laboratory Cu K_α 8.05	200^3	32.0	42.7

which can provide new scientific insights to help address these issues.

Several characterization and analysis methods that have been developed, adapted, or used to characterize the porous nickel (Ni), yttria-stabilized zirconia (YSZ) cermet (i.e., ceramic-metal mixture) SOFC anode in previous studies are discussed in detail in this work [1,2,24,25]. Specifically, those properties that are representative of the volume, including the details of the formulation and implementation of methods, are discussed here. A second and complementary part to this work provides details regarding some quantitative methods developed to provide detailed descriptions of the microstructure and how this relates to transport processes that the structure must support [3]. These methods are described in the context of the SOFC porous Ni–YSZ anode structure, which is the focus of the authors' efforts. The methods may also be amenable to other scientific communities and characterization methods, like the dual beam focused ion beam scanning electron microscopy (FIB-SEM) measurements that have been reported within the community [26–28].

2. Samples and methods

2.1. SOFC samples and preparation

Several samples, taken from anode-supported microtubular SOFCs, are considered. X-ray computed tomography (XCT) methods have been used to image and reconstruct the details of two unique but related methods for this process [1,2]. In total, three samples have been imaged and reconstructed, which are discussed in this work.

The three samples that are used in this work have been sectioned from an anode-supported microtubular SOFC so that they could be imaged, reconstructed, and segmented. The SOFC did not have a cathode or current collectors at the time of sectioning. The sample is comprised of a porous Ni–YSZ cermet anode, where an 8 mol% Y_2O_3 doped ZrO_2 form of YSZ is used. Ni in the anode is a reduced from the NiO used during fabrication. The electrolyte is a dense YSZ film. All of the samples have nearly even volumetric ratios of Ni and YSZ in the anode support. The anode support and electrolyte have a thickness of several hundred and several microns, respectively. Two of the samples are from the anode/electrolyte interface region, and the third is from the anode support.

2.2. Sample X-ray computed tomography

Imaging of the SOFC anode microstructure, and the subsequent reconstruction, have been made on two separate XCT systems. The first sample, Sample ID 1, has been imaged using a transmission X-ray microscope (TXM) with a synchrotron based hard X-ray source. More complete details on the imaging methods, equipment, reconstruction algorithms, and limiting factors are reported elsewhere [1,2,29–34].

The two remaining samples, ID 2 and ID 3, have been imaged using a bench-top XCT system with a laboratory Cu K_α X-ray source. The methods that are used to image these samples are also consistent with those reported in the literature [2,29]. Two important distinctions with the analysis of these samples are that they maintain a 42.7 nm spatial resolution and the elemental phases cannot be uniquely distinguished with the method due to the use of a single X-ray energy level with a laboratory Cu K_α X-ray source (8.05 keV). Only the dense and pore phases are uniquely resolved with these methods.

To distinguish the individual samples, they are noted along with sample identification numbers in Table 1. Table 1 provides a breakdown of the samples considered, and the corresponding methods used for their imaging and characterization as they are referred in the proceeding sections. The characteristics of each of these samples are provided in Table 1, including their location with respect to anode and anode/electrolyte interface, elemental phases examined, and the X-ray source used during analysis. Table 1 also provides descriptions of the number of voxels, or 3-D cubic elements inferred during the tomographic reconstruction process, the edge length of the pixels used to reconstruct these voxels, and the spatial resolution of the measurement. The spatial resolution is based on the Rayleigh criterion.

Sample ID 1 is the only sample that makes distinction of the Ni-elemental phase in the dense regions of the heterogeneous porous sample. Elemental phase specificity has only recently been accomplished and was achieved by exploiting its spectroscopic X-ray absorption properties [1]. The Ni-elemental sensitivity has been achieved by utilizing the energy tenability of the synchrotron source.

2.3. Supplemental phenomenological samples

Several structures are artificially generated using Monte Carlo, or sphere-packing methods. These structures are used to supplement the imaged samples. The sphere-packing method is used to artificially generate three-phase heterogeneous structures. Similar approaches have been explored by a number of groups for the purpose of trying to replicate the electrode architectures on a numerical basis. Works by the groups of Sunde, Brandon, and Costamagna are just a few of the examples within the SOFC community whom have used sphere packing, Monte Carlo, and percolation theory based approaches [35–43]. Significant insights and contributions to the SOFC and broader scientific community have been provided by these methods; however, the ability of these methods to uniquely replicate real electrode structures is difficult to validate. This uncertainty is a product of the non-linear processes that the structures support, permutations of the possible structures, and limited methods available to uniquely validate these approaches.

Assumptions about the nature of the physical structures that are being replicated are required to use these methods. These assumptions are used to condition these types of sphere-packing methods and are limited by our present understanding of the systems. Detailed reconstructions of real structures using XCT, FIB-SEM, and other stereological reconstruction and imaging methods can provide great insight into how to better replicate real structures using these types of artificial generation. Torquato's reviews [44–46] on the use of stochastic correlation functions to measure real het-

Table 2
Properties of generated phenomenological structure and grid.

Phase	Volume fraction	Set particle diameter, μm	Particles	Voxel size, nm^3	Voxels/Edge	Volume, μm^3
Ni	0.330	1.0	95	50^3	–	–
YSZ	0.329	1.0	165	50^3	–	–
Pore	0.341	NA	–	50^3	–	–
Volume	1.00	NA	–	50^3	100	5^3

erogeneous multifunctional structures and subsequently replicate them are widely discussed in the literature.

Due to the difficulty in trying to validate artificially generated structures, a reverse approach is used. Structures generated for this study are considered phenomenological; they are only used as a framework for the development and demonstration of quantitative characterization tools and approaches. The sphere-packing routine used in this study considers the random placement of N_{YSZ} spherical YSZ particles and N_{Ni} spherical Ni particles of diameter, D_{YSZ} and D_{Ni}, respectively, in a cubic volume of L^3. The cubic volume is broken down into cubic voxels of comparable dimensions to the experimental XCT data for consistency. Voxels that are 50 nm per edge with volumes comprised of 100 voxels per edge are considered in this study. The YSZ particle placement is randomly generated within this volume. It is completed prior to the random Ni particle placement. The Ni particles are permitted to overwrite the YSZ particles, as well as other Ni particles. To provide appropriate volumetric contributions of all three phases, more YSZ particles are initially placed within the volume.

More sophisticated approaches are possible, but the described method is suitable for the purposes of this work. Details of the generated structures are provided in Table 2, where $D_{Ni} = D_{YSZ} = 1.0$ μm particles are used, which are reasonably typical of present SOFCs. Fig. 1 provides renderings of the contiguous regions of the 3-D phenomenological sphere-packing structures generated for this study. Incremental subsets of this structure are rendered, as will later be used to demonstrate the volumetric dependencies of the various interfaces that are measured for this volume. These subsets are 1^3 μm^3, 2^3 μm^3, 3^3 μm^3, 4^3 μm^3, and 5^3 μm^3 in total volume. Regions that may appear disconnected are an artifact of the rendering process. Additional structures are considered in Part 2 of this study [3].

3. Characterization methods

3.1. Mercury intrusion porosimetry

Mercury intrusion porosimetry (MIP) experiments are performed on neighboring regions of the samples that were imaged using XCT methods. The MIP experiments are performed as a means to provide an independent experimental validation to several of the measurements made in this two-part study. The methods that are used to perform the MIP experiments are detailed here, with additional information available in [47]. The MIP experiments provide the volumetric distribution of the pore regions within these samples. This information is used for demonstration and validation purposes with respect to the reconstruction and characterization methods.

3.1.1. Experimental

The MIP experiments are performed using a Quantachrome PoreMaster-60. Separate chambers available for low- and high-pressure analyses are used. The absolute pressures for these chambers fall in the range of 6.9×10^3 N m^{-2} (1 lb in^{-2} absolute) to 3.5×10^5 N m^{-2} (50 lb in^{-2} absolute) and 1.4×10^5 N m^{-2} (20 lb in^{-2} absolute) to 4.1×10^8 N m^{-2} (60,000 lb in^{-2} absolute), respectively. The maximum pressure for the chambers is manually adjusted. The mercury serves as a non-wetting fluid to the porous sample, providing the ability to examine the sample's small pore diameters. A pressure gradient must be applied to force mercury into the pores of the sample. The pressure required to intrude a pore of diameter, D, was predicted using the Washburn equation [47,48]. The properties required for this analysis are the mercury surface tension, $\gamma = 480$ dynes cm^{-1}, and the contact angle, $\theta = 140°$.

To perform the MIP experiment, a sample is placed in a penetrometer which contains a bulb for holding the sample. The penetrometer is connected to a column that is used for measuring the change in the level of mercury outside of the sample. High vacuum grease is applied to the lip of the penetrometer to create a seal with an electrode that is used to electronically measure the mercury level. Each penetrometer is calibrated so that the change in the level of mercury can be measured and used to calculate the intruded volume. To prepare the experiment, the cell is evacuated and subsequently filled with mercury, surrounding the sample. The cell containing the sample and mercury is returned to ambient pressure. The parameters for the experiment are selected, where the motor speed is set to the lowest value of, 1, which corresponds to a maximum pressure ramp rate of 4.1×10^6 N m^{-2} min^{-1}

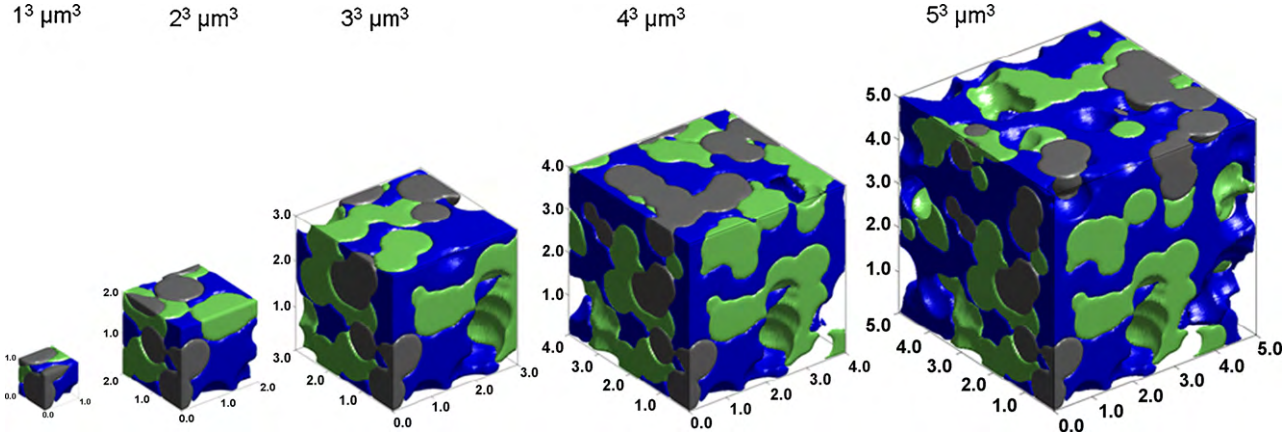

Fig. 1. A 3-D rendering of a phenomenological sphere-packing structure considered in this study, where the Ni (grey), YSZ (green), and pore (blue) are shown as subsets of a 5 μm × 5 μm × 5 μm cubic volume used for determination of volume independence. Only the contiguous regions are shown. (For interpretation of the references to color in this figure legend, the reader is referred to the web version of this article.)

($600\,\mathrm{lb\,in^{-2}\,min^{-1}}$), and the pressure range was specified to run from absolute pressures of $1.4 \times 10^5\,\mathrm{N\,m^{-2}}$ ($20\,\mathrm{lb\,in^{-2}}$ absolute) to $2.1 \times 10^7\,\mathrm{N\,m^{-2}}$ ($3000\,\mathrm{lb\,in^{-2}}$ absolute). The pressure range represents pressures that are sufficient for the detection of the pertinent pore diameters while also remaining low enough that the brittle samples are not destroyed by the pressure. Other inputs included the penetrometer volume, calibration constant, contact angle, surface tension, mercury density, and the total volume of the sample. The total volume of the sample is calculated using the sample weight and is further used for normalization of the experimental data. During the experiment, the pressure is incrementally increased and the cumulative volume intruded into the sample was measured at each incremental pressure. Recalling, that the pressure is related to the pore diameter through the Washburn equation, the cumulative intruded volume is recorded and can be presented in terms of pressure or the pore diameter.

3.1.2. Data interpretation

Using the described experimental practices, the pressure and intrusion volume data collected from the MIP experiment are used to calculate the normalized phase size distribution (PSD) function, $\alpha_n(D)$, for the pore phase. This distribution function provides the normalized volume of mercury contained by a specific pore diameter and is the basis for the structural parameter calculations. The normalized pore–PSD function is defined as the volume of mercury intruded into a range of pores of diameters, ΔD, centered at a pore diameter, D, normalized by the total volume of the sample and divided by ΔD. The units of α_n are thus inverse length (i.e., $\mu\mathrm{m}^{-1}$). The pore–PSD, $\alpha_n(D)$, is obtained by numerically differentiating the intruded volume of mercury with respect to the pore diameter and is normalized by the total sample volume.

$$\alpha_n = \left(\frac{1}{V_T}\right)\frac{dV}{dD} \tag{1}$$

While discrete, the pore–PSD developed by the intrusion process must be considered continuous to assist in the development of equations for interpreting pore volume fraction, $\left\langle V_{\mathrm{Pore}}/V_T \right\rangle$, pore tortuosity, τ_{Pore}, and so forth; however, the derivative that represents the differential pore diameter must be taken discretely from the MIP data.

With the pore–PSD, the microstructural parameters mentioned previously are calculated. The pore volume fraction, $\left\langle V_{\mathrm{Pore}}/V_T \right\rangle$, is calculated by numerically integrating α_n with respect to the differential diameter, over all diameters.

$$\left\langle \frac{V_{\mathrm{Pore}}}{V_T} \right\rangle = \int_0^\infty \alpha_n \, dD \tag{2}$$

Similarly, a representation of the tortuosity of the sample's porous regions can be developed using the pore–PSD analysis. This is achieved by considering the intrusion into the pores as a viscous flow through channels of diameter, D, and effective length, $L_{\mathrm{eff}}^{\mathrm{Pore}} = \tau_{\mathrm{Pore}} \cdot L$. In this manipulation the varying pore diameters are treated using the normalized pore volume distribution function, α_n, shown in Eq. (1). With this approach, the total free stream flow rate that is fed into the pores creates a uniform pressure drop across the porous media. The relation for laminar flow head loss in a pipe was then used to relate the pressure drop divided by the unknown pore velocity, to the pore effective length, $L_{\mathrm{eff}}^{\mathrm{Pore}}$. Independently, the Ergun equation can be used to correlate the ratio of the pressure drop to the upstream velocity across the porous media [49]. The upstream and pore velocities must be related through continuity to do so. The pressure drop divided by upstream velocity can be used in the relation for head loss to calculate $L_{\mathrm{eff}}^{\mathrm{Pore}} = \tau_{\mathrm{Pore}} \cdot L$ and allows for the solution of tortuosity, τ_{Pore}.

$$\tau_{\mathrm{Pore}} = \sqrt{\frac{2.083}{(D_H)^2 \cdot \left\langle V_{\mathrm{Pore}}/V_T \right\rangle} \int D^2 \alpha_n \, dD} \qquad \text{where}$$

$$D_H = \frac{\left\langle V_{\mathrm{Pore}}/V_T \right\rangle}{\int (1/D)\alpha_n \, dD} \tag{3}$$

A more complete discussion on the formal definition of the tortuosity and its implication on transport are provided in Section 3.4.

3.2. Volume fraction

Elemental phase and pore volume fractions are examined in several studies which provide detailed 3-D descriptions of the electrode microstructure, both by the authors' and other groups [2,24–28]. For completeness, the volume fraction of a given phase or pore is defined as the ratio of the volume of that phase within the sample to the total sample volume. These methods have been discussed elsewhere and have importance to issues such as percolation limits in multi-phase heterogeneous structures. For the volume fraction measurements made on segmented and reconstructed XCT data, the 3-D morphology is comprised of cubic voxels of a finite size and an individual phase designation (pore, Ni, or YSZ). Voxel counting routines are used to define the volume fraction of each phase.

3.3. Contiguity

3.3.1. Conceptual development

The contiguity, or volumetric connectivity, of the individual phases is of importance to understanding the heterogeneous structure's functional behavior. A numerical algorithm is used to assess the contiguity of the considered samples and structures. This algorithm is conceptually represented in Fig. 2, using an arbitrary 2-D structure. In Fig. 2(a), the phase of the structure being examined is shown in white and designated with a 1. All secondary phases, or regions, of this structure are shown in black and designated with a 0. To identify the contiguity between the left and right faces, it is necessary to identify regions that maintain blind, or dead-end, phase paths from the left and right faces in addition to regions of isolated phase. Examples of these regions are called out in Fig. 2(a). The top and bottom boundaries are assumed insulated. A numerical painting scheme is used to interpret the contiguity. The conceptual basis of the numerical painting scheme is illustrated in Fig. 2(b) through Fig. 2(d). The scheme works by starting from the left face and marching through the structure. During this marching process, all 1's that are connected to the left face through other 1's are replaced with 2's. This process is accomplished by recursively sweeping through the structure. During these sweeps, any voxel that is denoted with a, 1, and has a face in contact with a voxel with a value of, 2, is updated as a, 2.

Following this update, a similar process is completed from the right face propagating towards the left face, with all 1's and 2's that are connected to the right face being replaced with 3's as shown in Fig. 2(c). Finally, as shown in Fig. 2(d), a fourth process propagates from the left face to the right face of the structure replacing all of the 3's that are connected through the left face with 4's. When complete, the contiguous structure is denoted with 4's. All isolated regions are denoted as 1's and blind regions from the left and right face are denoted as 2's and 3's, respectively. Because each voxel has a finite and consistent volume, the percent of the total volume associated with the contiguous, left blind, right blind, and isolated regions can be determined. As illustrated in Fig. 2(e), a clean

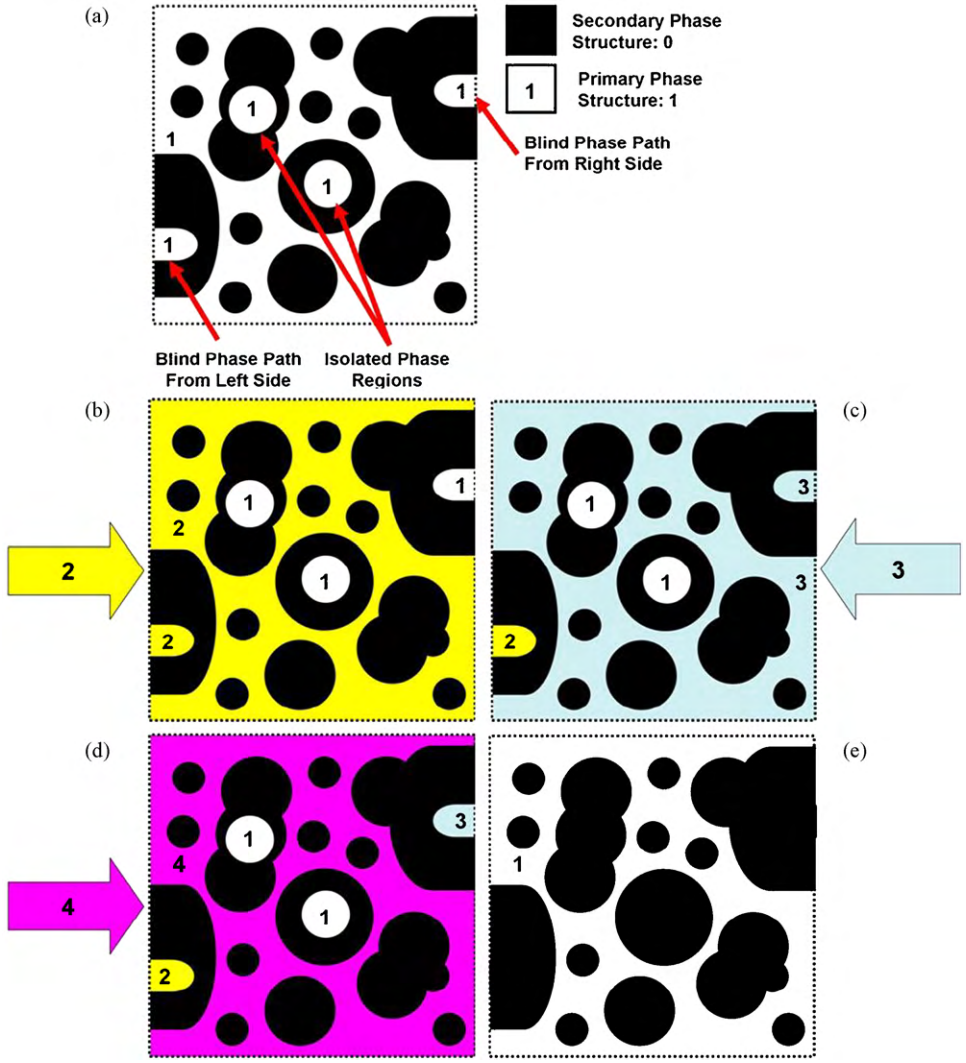

Fig. 2. A 2-D representation of the contiguity measurement algorithm. The initial structure, (a), is shown with the white region being studied is set as a 1. Starting from the left face (b), all of the connected 1's are replaced with a 2. Subsequently, (c) all of the 2's and 1's connected to the right face are replaced with 3's. Returning to the left face, (d) all of the 3's connected to the left face are replaced with a 4. Non-contiguous regions are left with numerical designations of 1, 2, and 3, which (e) can be removed for subsequent analysis.

numerical structure that only maintains contiguous pathways can be produced, which will be used in other analyses.

3.3.2. Numerical methods

The contiguity measurements are straight-forward to make; however, there are several clarifications. First, these measurements have been described for a 2-D structure. The extension of these methods to 3-D samples is straight-forward. The key differences are that the 3-D structure is more numerically intensive to examine and that all of the adjacent side faces must be insulated. When multiple phases are present within the structure, each considered on an individual basis. Finally, the numerical painting process described operates through the consideration of the numerical values of neighboring cells extending from a plane. In practice, this is carried out by iteratively sweeping through the structure and updating neighboring cells. Because of the large data sets in the 3-D structures (e.g., order of 10^6 to 10^7 integer values for the samples considered), recursive data sweeps and careful data management are required to obtain a solution while also minimizing the computational cost.

The structure is numerically searched for the numerical indicator of the phase being examined, which was used during the previous iteration. For example, while painting the structure with 2's, the structure is searched for 1's. As a 1 is identified, all of the voxels sharing a face with this voxel are checked to see if a 2 is present. If a 2 is present, the corresponding voxel is updated. This process is repeated throughout the structure for each operation until no additional numerical updates occur.

3.4. Tortuosity

The tortuosity of the porous regions of the sample can be defined with methods like MIP, as discussed in Section 3.1. It can also be evaluated by using numerical methods which can examine the segmented and reconstructed sample morphology. Several of the authors' previous studies have considered the pore–phase tortuosity or an empirical factor, Ψ, which is representative of the influence of the structure on transport [2,25]. Here, we expand upon the definition of the tortuosity, prior to expanding upon the methods used in this study.

3.4.1. Representation of tortuosity

A phenomenological, 3-D representation of the tortuosity is provided for a single path in Fig. 3. This path represents an arbitrary

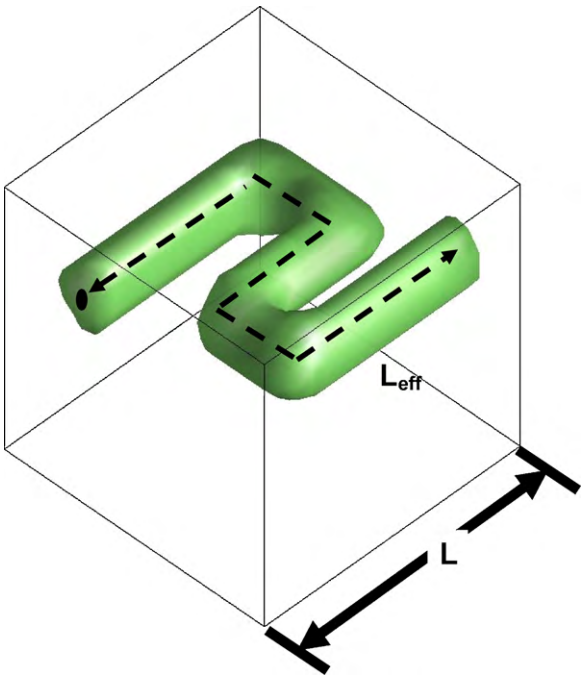

Fig. 3. A 3-D representation of the tortuosity, where the tortuosity is defined as, $\tau = L_{\text{eff}}/L$, where the effective path length, L_{eff}, and nominal volume length, L, are noted.

phase path that may exist in a sample. Following the path's centerline, an effective path length, L_{eff}^{ϕ}, is identified. The ratio of the effective path length to the nominal edge length of the same volume, L, allows the tortuosity, τ_ϕ, for phase, ϕ, to be defined.

$$\tau_\phi = \frac{L_{\text{eff}}^{\phi}}{L} \tag{4}$$

The tortuosity can be confused with the tortuosity factor, κ_ϕ, for porous media, where the tortuosity factor is the square of the tortuosity [50–53].

$$\kappa_\phi = \tau_\phi^2 = \left(\frac{L_{\text{eff}}^{\phi}}{L}\right)^2 \tag{5}$$

In many empirical transport models, the tortuosity factor, and thus the tortuosity, plays a key role in describing the structure. These models treat the structure as a homogeneous, or an effective medium, which is dependent upon the tortuosity factor. For mass transport in a porous electrode, this is achieved by scaling the Fickian diffusion coefficients, with the ratio of the pore volume fraction to the tortuosity factor as shown in Eq. (6). However, as has been noted by Epstein [50] in an examination of some classic empirical correlations for porous media, reviewed by DeCaluwe et al. [51], and observed in practice by Schmidt and Tsai [52]; the discrepancy between the tortuosity and tortuosity factor is often been misinterpreted.

Examining several publications that describe the effect that the structure has on transport processes [50–53], an empirical relationship for the correction for transport coefficients in porous media is identified. For Fick's law, this correction,

$$\vec{J} = -\frac{\langle V_\phi/V_T\rangle}{\kappa_\phi} D\nabla C = -\frac{\langle V_\phi/V_T\rangle}{{\tau_\phi}^2} D\nabla C \tag{6}$$

is used to describe molecular diffusion in the pore–phase, generically labeled phase, ϕ. This correction is readily extendable to the Stefan–Maxwell and Dusty Gas equations. Because Eq. (6) was presented for mass transport in the pore phase, $\vec{J}$ represents a molar flux, D the molecular diffusion coefficient, $\langle V_\phi/V_T\rangle$ the pore volume fraction, and ∇C the molar concentration gradient.

This permits the interpretation of an empirical diffusivity factor, Ψ_ϕ, which is a property of the material and therefore represents the structure as an effective homogeneous material.

$$\Psi_\phi = \frac{\langle V_\phi/V_T\rangle}{\kappa_\phi} = \frac{\langle V_\phi/V_T\rangle}{\tau_\phi^2} \tag{7}$$

By analogy, the diffusivity factor could also be extended to other transport processes including electronic, ionic, or heat conduction processes in the solid phases.

3.4.2. Numerical methods

The methods and algorithms used to determine the tortuosity of the individual phases are described here. Fig. 3 provides an overly simplified representation of the tortuosity. In actuality, multiple contiguous pathways are likely to exist. These pathways through a given phase can branch, merge, dead-end, have connected regions of different cross-sections (i.e., constrictions), and exhibit some degree of anisotropy. This complexity highlights a need for simplifications, which can provide properties that are representative of the complex heterogeneous structure. However, it must be recognized that the effects of these details can be lost in such a representation.

The tortuosity is evaluated using a numerical method described by Joshi et al. [25], which is an extension of a method that has been used by Wilson and Barnett [27]. These methods use a finite difference method to solve Laplace's equation. The solution to Laplace's equation is then used to back out the tortuosity of the structure. Joshi et al. [25] modeled diffusion in the 3-D pore–structure of several samples. In this analysis, a pore diffusivity factor, Ψ_{Pore}, is identified by taking the area weighted integral averaged flux for the 3-D structure relative to that of a 1-D solution to Laplace's equation, where the structure is approximated by a homogeneous equivalent structure. The diffusivity factor, Ψ_{Pore}, is an empirical representation of the effects that the detailed structure has on the 1-D analysis. It is consistent with the details provided and discussed with Eqs. (6) and (7). The diffusivity factor is evaluated in three principle (X, Y, Z) Cartesian directions of the cubic volume. The boundary conditions and numerical methods are provided in these studies. Joshi et al. [25] left the diffusivity factor as a bulk empirical parameter. Here, the tortuosity are explicitly identified by equating the calculated diffusivity factor, Ψ_ϕ, with Eq. (7).

3.5. Interface measurements

The digital representation of the sample's morphology provides a convenient framework for the examination of the pore, Ni and YSZ interfaces. This is permitted by the binary representation of the structure in the form of voxels. These voxels are of consistent and finite scale and contain an individual elemental phase designation.

To understand these measurements, a phenomenological representation of the three-phase boundary (TPB) line and two-phase area interfaces for individual sets of voxels is provided in Fig. 4. In Fig. 4(a), the unit line length that is formed by the union of the voxels of the three constituent phases is provided, as indicated by the arrow. An important aspect of the TPB line is that for a right-handed coordinate system the unit TPB line projects normal to the plane. Fig. 4(b) shows four voxels as they may appear in the generated structures or the reconstructed morphology of the XCT data. As the faces along which these voxels merge are inspected, two-phase interfaces can be distinguished between two voxels of discrete phases and finite size. These simplified representations demonstrate how the 3-D morphology can be examined for interfaces.

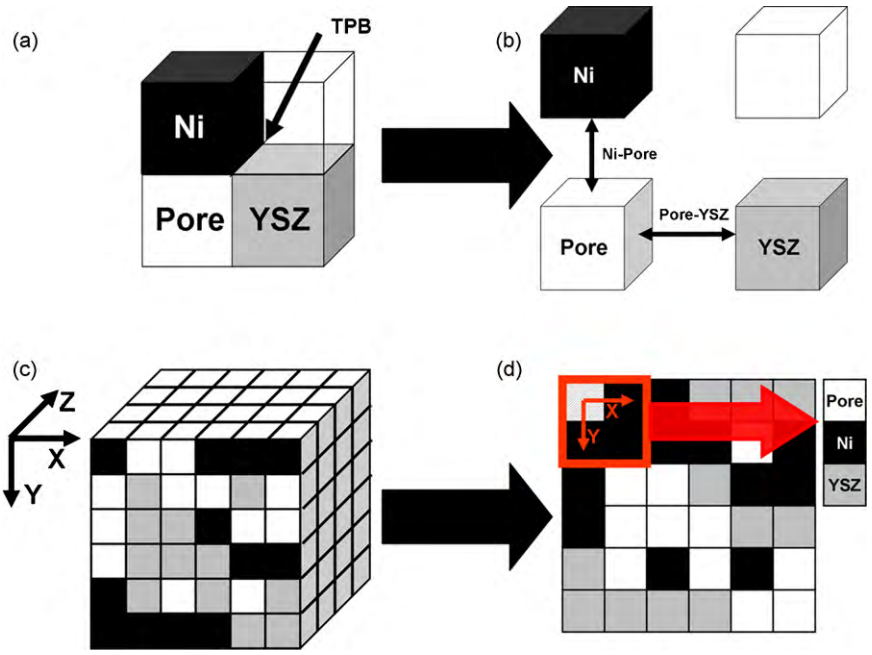

Fig. 4. The (a) three-phase-boundary line occurring at the union of three voxels of unique phase, and (b) area forming the two-phase interfacial lies along the faces of two unique voxels. The 3-D digital structure (c) is searched, using (d) an individual 2-D plane in this 3-D structure.

Extending these concepts to the 3-D morphology, a numerical algorithm is used to search and track these interfaces. A simplified representation of how this method works is provided in Fig. 4(c) and (d). To identify TPB lines, we begin at the top left of the front of the cubic volume shown in Fig. 4(c). This region is denoted with the principle axis. For this first 2-D plane (i.e., the first row of the *X*–*Y* plane), a conceptual representation of a plane is shown in Fig. 4(d). This plane is iterated through, progressing in the positive *X*-direction from the *X*–*Y* origin. Iterating through this row, the phase associated with the voxel at each node is identified. This is denoted in Fig. 4(d) with a cross-hatching of the voxel noted with the axis. While at this voxel, the phase associated with the voxels in the incremental positive *X*, *Y*, and *X*–*Y* direction are identified. In Fig. 4(d), these voxels are enclosed with a bold box. As the phases associated with these voxels are identified, they are checked to see if all three-phases exist. As shown, there is not a TPB in the four voxels being examined; however, if there were a TPB, it would extend into the page by the unit voxel length. Each TPB is counted as it is identified.

As we continue the search for the TPB elements, we move to the origin voxel and the voxels being checked by an increment in the $X+1$ direction. This is shown by the large arrow in Fig. 4(d). This process continues until we are one voxel from the edge of the cubic volume in the *X*-direction. At this time, this row is completed and we move over the next row in the $Y+1$ direction back at the initial *X* value. This process continues until the entire *X*–*Y* plane has been examined. Once an *X*–*Y* plane is complete, the subsequent *X*–*Y* plane in the *Z*-direction is examined in a similar manner and the process is repeated until every *X*–*Y* plane in the cubic structure has been searched. While it may seem as if the entire structure has been searched, in actuality only the TPB lines that lie parallel to the *Z*-direction have been identified at this point. This is because only TPBs in the incremental positive *X*, *Y*, *X*–*Y* directions were examined in each plane of the *Z*-direction. For this reason, a similar analysis is also completed through the structure in the *Y*–*Z* and *X*–*Z* planes. The double-counting of a unit TPB interface is avoided in this analysis procedure by always iterating and evaluating neighboring voxels in the positive direction. Once the TPBs have been counted, they can be converted to a physical length using the unit voxel edge length. The TPB length identified must be normalized by the volume of the sample considered so that it can be reported as a property of the sample.

To identify the two-phase interfacial areas, a similar numerical algorithm is used. Iterations through all of the planes are required; however, for each voxel, only the nearest neighbor in the same row is considered (i.e., *X* to $X+1$). Incremental increases in the areas must be tracked for each type of phase interface: Ni–YSZ, Ni–pore, and YSZ–pore. Searching the neighbor in the positive direction, relative to the search direction, avoids the double counting of the interfaces. All three planes are searched and the measured phase-interface areas are normalized by the volume of the sample.

An extension of the interface measurement can also be proposed that considers only those interfaces that maintained contiguous transport pathways through the structure. The treatment of this modified form of the interface measurements is handled through the use of the contiguity algorithms (Section 3.3), in conjunction with the interface measurement algorithms. For this modified form, each phase is separated into a unique structural file and examined using the contiguity measurement algorithms. Non-contiguous regions are tagged so they are not considered as a part of any individual phase. A geometric file considering the full phase-specific morphology is reconstructed using these contiguous descriptions of the phase-structures. The TPB and phase-interface areas are again examined using the algorithms described above to identify their values where there is continuity through the respective phases.

3.6. Measurements on heterogeneous structures

How the heterogeneity of the samples impacts the methods and measurements performed in this study is an important consideration. If a small sample volume is considered, the properties that are measured for this volume may be substantially different from those in a neighboring region of the sample. This type of scenario is supported by Fig. 1, where one may expect to obtain different characteristic properties for a 1^3 μm^3 volumes than say the 5^3 μm^3 volumes—even for the same original volume. If a sufficiently large volume is considered, these values may asymptote and become

independent of the volume considered. Such an observation can occur when localized changes are outweighed by those of the bulk sample volume.

The approach taken to demonstrate volumetric independence is highlighted in Fig. 1, where five sub-volumes of the same 5^3 μm^3 volume generated for this study are shown. These sub-volumes may be viewed as "Russian stacking dolls" of the same structure; they are incremental volumetric increases of the same structure. Measurements are made on each of these sub-volumes to observe volumetric dependencies. If a given measurement continues to change with increasing volume, it would be indicative that each measurement is representative of that particular volume considered. However, if the changes in a measurement asymptotically approach zero with increases in volume, it indicates that the measurement is representative of the sample. Different regions in a large sample can still maintain unique properties. This is often recognized in electron- and optical-microscopy, where neighboring regions of the same specimen can appear quite unique. These types of effects are beyond the scope of this work. They can be treated on a statistical basis through the processing of multiple sample regions from the same original microstructure.

In attempt to understand the volumetric dependencies of the measurements made in this study, sub-volumes of the full structures are examined. As demonstrated in Fig. 1, we begin with a small subset of this data (e.g., a 1^3 μm^3 sub-volume). The size of this sample sub-volume is incrementally increased until the full volume is considered. At each increment, the measurements are re-examined and the volumetric dependence of the sample is tracked. The measurement can only be considered as representative of the sample when it can be shown as independent of the volume which is considered.

4. Results and discussion

4.1. Mercury intrusion porosimetry

Experimental results from mercury intrusion porosimetry (MIP) experiments have been reported in several previous studies by the authors [2,47]. In these studies, the MIP experiments are used to determine properties of the heterogeneous electrode structure, such as the mean pore radius, porosity, and tortuosity [47], and to validate XCT based characterization methods [2]. The pore volume fraction, tortuosity, and mean pore radius determined by the MIP measurement of Samples ID 2 and ID 3 can be used to validate values determined using the reconstructed XCT microstructures. The pore size distribution spectra determined using the MIP data also provides a point of comparison for the PSDs developed using the reconstructed XCT microstructures in Part 2 [3].

The MIP pore–PSD results for Samples ID 2 and ID 3 are provided in Fig. 5. These results show the normalized volumetric contribution of a pore of diameter, D, within the sample. This pore–PSD is presented as a power spectrum and maintains units of inverse length (μm^{-1}). Conceptually, it represents the volume fraction of the pore regions within the sample that maintain a diameter, D, over a differential diameter, ΔD. Examining Fig. 5, it is recognized that Sample ID 2 maintains much more of its volume at smaller pore diameters, down to sub 0.1 μm pores, with the largest contribution coming from pores of approximately 0.5 μm in diameter. Sample ID 3 maintains a larger portion of its volume at larger pore diameters, with a very significant peak at approximately 0.6 μm in diameter.

Several aspects of the MIP method can lead to misinterpretations of the pore structure. We begin by recognizing that the method is intended to provide a quantitative measure of the complete pore structure; however, it actually provides a quantitative

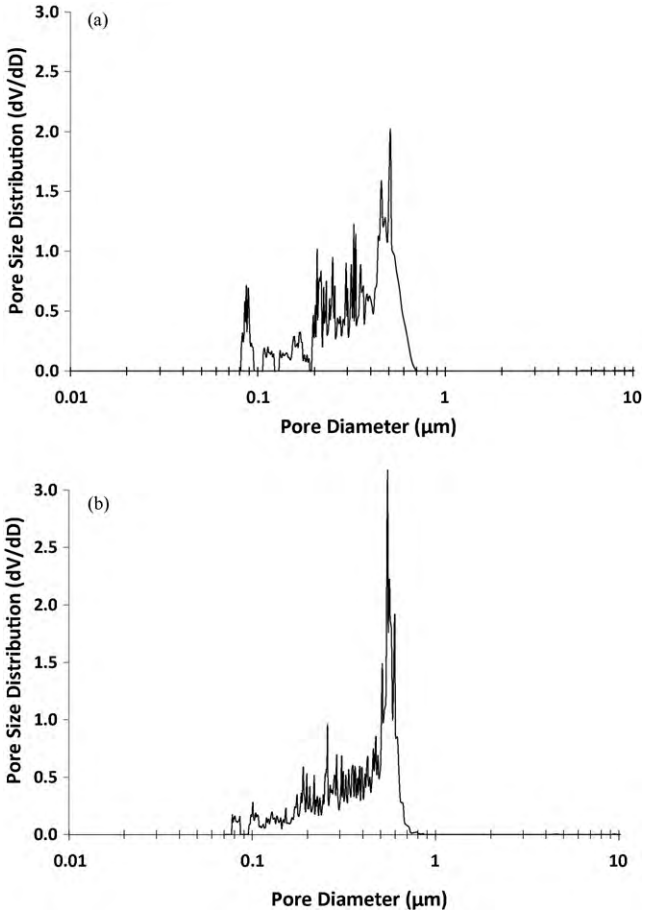

Fig. 5. Pore phase size distribution obtained with mercury intrusion porosimetry for pore regions of (a) Sample ID 2, and (b) Sample ID 3. The distributions have units of μm^{-1}.

measure of the throats of the pore. This occurs because the porous media is treated as a group of independent capillaries. As demonstrated in Fig. 6, pores are more likely to merge, split, and have blind (or dead-end) paths. Due to our limited ability to describe the structure, the volume intruded at a given pressure is attributed to pores of that diameter. If there is a pocket or larger region behind the throat of a pore, this volume will be attributed to pores of the

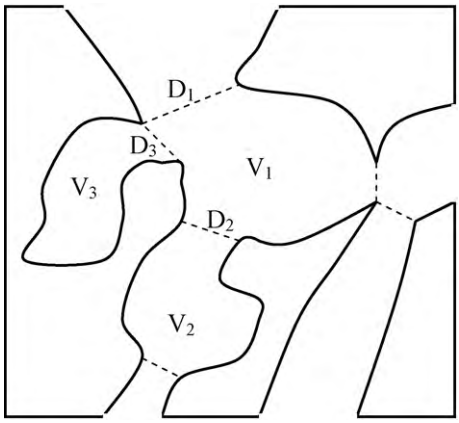

Fig. 6. A schematic of the heterogeneous porous media, as interpreted by mercury intrusion porosimetry. Three pore regions, of volume, V_i, are attributed to the pore's throat diameter, D_i.

diameter of the pore throat because the pressure necessary to force mercury into these larger void regions is less than that through the throat of the pore. Once the pressure can force mercury through a given pore throat, it will fill the region behind it. In effect, this weights the pore–PSDs toward the smaller diameters, which correspond to the throats of the pore structures. Similarly, multiple runs are often used to verify the pore–PSDs. Mercury trapped in the structure and/or mechanical degradation due to the pressure exerted on the sample can affect the measurements. For the cases reported in this study, two intrusions were performed on each sample. Data from the first was used in the analysis. The second intrusion was used to verify the intrusion and that there was not mechanical degradation, which could result in significant variations in the pore–PSD. Minimal changes were recognized for both samples considered in this study.

4.2. Volume fraction

The methods used to identify the volume fraction of the phases within the sphere-packing generated structures and the XCT based samples are the most straight-forward discussed in this study. These measurements are based on voxel counting algorithms. The volume fractions of the sphere-packing generated structures and actual samples considered in this work are provided in Tables 2 and 3, respectively. It is noted that the values recognized in Sample ID 1 are likely different than those of the bulk sample, as a result of the small volume available for study and its proximity to the dense electrolyte.

Because large differences can be observed in localized regions, as is likely the case with Sample ID 1, it is important to demonstrate the heterogeneous nature of the samples and an ability to demonstrate volumetric independence. These efforts are undertaken for the pore regions of Samples ID 2 and ID 3 in Fig. 7. Volumetric independence is observed for volumes larger than 4 μm per edge, or 4^3 μm^3. Sample ID 2 appears to decline as it approaches a volume of 6 μm per edge, or 6^3 μm^3; however, this is due to the inclusion of a region of the dense electrolyte in the larger sample volumes. Although the volumetric independence for the pore volume fractions of the two samples considered in Fig. 7 is recognized for a volume of approximately 4^3 μm^3, other properties including volume fractions of the dense phases can and will have unique volumetric dependencies.

4.3. Contiguity

Of direct relation to the phase volume fraction, is the contiguity of these regions. The contiguity is defined as the percentage of the same phase that is continuous, or interconnected, within the considered volume. Regions of a phase without a continuous path through the structure are non-contiguous. These regions can still contribute in terms of the structural stability; however, they do not contribute to its electrochemical performance in terms of electrocatalytic activity or the mass and charge transfer processes. Therefore, the contiguity may be considered as a measure of the effective use of the microstructure.

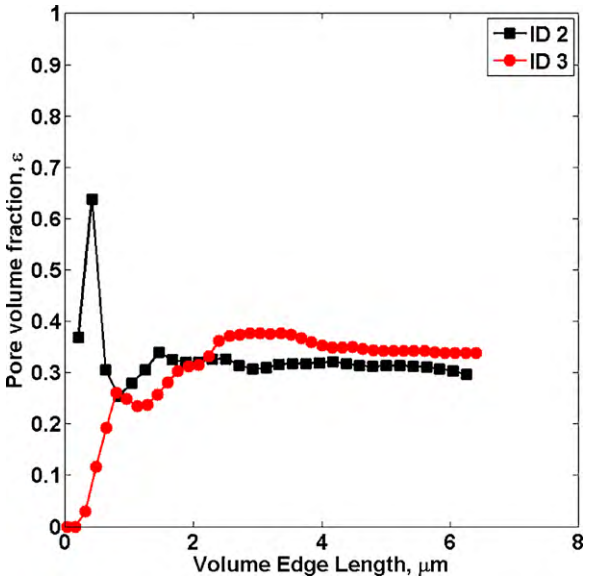

Fig. 7. The dependence of the porosity, ε, on the size of the volume considered is shown for Samples ID 2 and ID 3.

Prior to the implementation of the contiguity routines, several verifications of the numerical measurement methods are completed. First, simplified structures with known non-contiguous regions are generated and checked using the developed algorithm. Second, levels of recursion are both forced and incrementally increased with all samples to ensure that the same numbers of disconnected voxels were identified within the same volume with increased recursion. Third, the samples are mirrored and re-examined to validate the algorithm. Finally, the original and cleaned morphologies are rendered to inspect the structures.

The contiguity for the segmented and reconstructed samples is provided in Table 3. The volumetric dependence of the contiguity for the three phases of the sphere-packing generated structure, as well as that for the pore regions of Samples ID 2 and ID 3, are provided in Fig. 8. The contiguity of the sphere-packing structures is provided in Fig. 8(a). They are discussed here because they will be of consequence to the active two- and three-phase interface measurements discussed in the following sections.

The contiguity of the Ni, YSZ, and pore regions of the sphere-packing generated structure, shown in Fig. 8(a), exhibit some interesting behavior. The pore regions, which are those regions that did not have an YSZ or Ni particle written to the volume, exhibit nearly 100% contiguity, independent of the volume size. The YSZ regions, which were placed within the volume prior to the placement of the Ni particles, exhibits a slight decrease in contiguity with increasing volume, but does asymptote at a volume of approximately 4^3 μm^3. However, the Ni contiguity, which is the final set of particles randomly written to the volume and permitted to overwrite pore, YSZ, and other Ni regions, demonstrates a consistent decrease with increasing volume size. This behavior is unexpected, considering the Ni comprises approximately a third of the volume. These effects are considered to be a product of the sphere-packing

Table 3
Effective homogeneous properties of structures imaged using XCT.

Sample ID	Phase	Volume fraction	Contiguity, vol.%	Tortuosity [x, y, z, mean]	Mean diameter [3], μm
1	Ni	0.46	96.8	1.7, 1.2, 2.7, 1.9	1.07
	YSZ	0.36	99.4	2.2, 1.4, 1.7, 1.8	0.64
	Pore	0.18	93.2	1.3,1.2, NA, 1.3	0.26
2	Pore	0.32	98.2	1.6, 1.7, 1.8, 1.7	0.51
3	Pore	0.34	98.9	1.7, 1.4, 1.7, 1.6	0.63

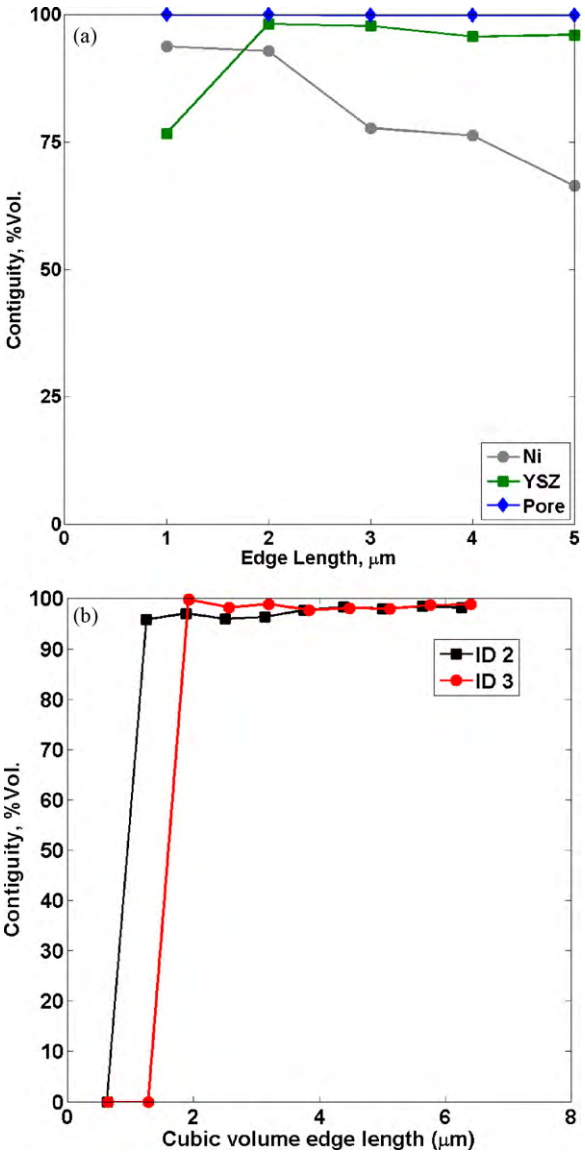

Fig. 8. The dependence of the (a) pore, Ni, and YSZ contiguity, or percent volumetric connectivity, on the size of the volume considered is shown for the sphere-packing generated structure, as is (b) the contiguity for the pore regions of Samples ID 2 and ID 3.

methods used for this work. These structures and results are only considered as phenomenological.

The pore regions of Samples ID 2 and ID 3, shown in Fig. 8(b), exhibit an asymptotic behavior for volumes of approximately 3^3 μm^3 and larger. The high contiguity suggests that the pore regions of these samples exhibit a high degree of connectivity and effective use. Similar studies are not shown for Sample ID 1 because the small sample volume makes it impractical to demonstrate these types of effects.

The contiguity measurements demonstrated in this section enable removal of non-contiguous regions from the structures analyzed. The modified structures are used in the tortuosity, interface, and transport studies for two reasons. First, non-contiguous regions can result in erroneous results in the tortuosity and transport studies. Second, only the contiguous regions contribute to the interfacial properties like the catalytic area, double layer area, and the electrocatalytic activity due to the three-phase boundary.

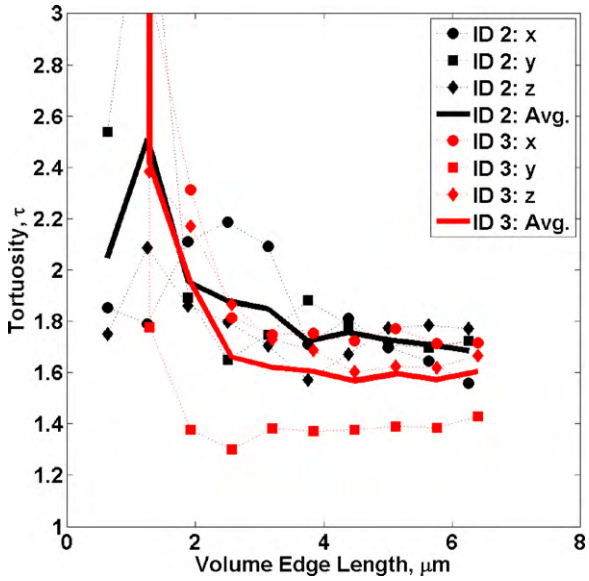

Fig. 9. The dependence of the tortuosity, τ, in the pore phase on the size of the volume considered is shown for Samples ID 2 and ID 3. The tortuosity is reported in the three principle Cartesian directions (symbols), as well as the mean value (solid lines).

4.4. Tortuosity

The tortuosity of the unique phases of the samples considered in this work is evaluated by solving Laplace's equation within the structure. This procedure is developed by considering diffusive mass transport in the pore regions of the sample; however, this approach can be extended to the dense Ni and YSZ phases, which support electronic and ionic conduction in the SOFC, respectively. This is achieved using an analogy between mass and charge transfer processes. The tortuosity for the detailed structures (i.e., Eq. (6)) can and should consider only the contiguous regions of the sample. Non-contiguous regions cannot support transport and therefore are not contributing to this factor. If a flux is applied to a non-contiguous region, a solution cannot be obtained as the numerical methods become unstable without a mass source/sink for these regions.

The algorithms and methods that are used to examine the tortuosity of the samples have been independently verified using simplified 2-D and 3-D structures. These simplified cases are not reported here in the interest of providing a concise discussion. The tortuosity can have a considerable influence on the efficiency of transport processes in heterogeneous structures. This is because the tortuosity, in effect, extends the length of the transport processes. Whether in the pore (mass), Ni (electronic), or YSZ (ionic) regions, an extended transport path length can increase the associated losses (i.e., irreversibility). This can occur both as a concentration loss due to a lower concentration of reactants at the TPB, and as resistive losses in the form of Joule heating through the heat produced by forcing a current through a material of finite resistivity over an increased length.

4.4.1. Tortuosity measurements

The tortuosity values for the segmented and reconstructed morphologies of Samples ID 1–ID 3 are provided in Table 3. In this table, the tortuosity measurements are reported for the three principle Cartesian directions. As with the previous two sections, it is important to verify volume independence of these types of measurements. In Fig. 9, the tortuosity for the pore regions of Samples ID 2 and ID 3 are shown. The mean tortuosity exhibits volumetric independence at approximately 4^3 μm^3 for both samples. As in the

preceding sections, Sample ID 1 does not maintain sufficient volume to demonstrate volumetric independence and therefore is not considered within the context of this study.

In Fig. 9, some additional scatter in the direction-specific tortuosity is noted in sample ID 3. This scatter is specifically associated with the *Y*-direction. It is possible this could be an artifact of the numerical methods; however, it is more likely the result of some anisotropy in the specific sample. Still, this is speculation at this point as we do not have a large enough statistical set to properly verify this assessment. The sample exhibiting this effect was taken from the support, where sample ID2 was taken from the interfacial region. The samples have been taken from unique anodes and regions, which may have unique properties. Multiple samples from a single anode will need to be considered in future studies so that a statistical set can be formed and the issues surrounding directional dependence and anisotropic effects can be better addressed.

4.4.2. Validation of tortuosity measurements

As a point of validation, the tortuosity values reported for the porous regions Samples ID 2 and ID 3, can be compared to those identified using independent experimental methods. In addition to the use of numerical methods to evaluate the tortuosity of the XCT data, the tortuosity of the pore regions of these samples is also examined using the MIP results. In Eq. (3) of the theoretical development, it is shown that the tortuosity of the porous regions of the sample can be measured with MIP by using the pore volume fraction distributions interpreted from the intrusion curves. Using Eq. (3), tortuosities of 1.7 and 1.8 are determined for Samples ID 2 and ID 3, respectively. These values agree remarkably well with the mean value of those identified by solving Laplace's equation for the XCT data, which were reported in Table 3 and Fig. 9. The tortuosity of the Ni and YSZ regions cannot be independently validated with methods like MIP. Therefore, the examination of the tortuosity of the Ni and YSZ phases represents an extension of the numerical methods presented to gain a new understanding of the heterogeneous structure. This is performed under the assumption that the numerical methods can be extended to these regions. There is nothing in the approach to suggest this is not an applicable extension.

4.5. Interface measurements

The final measurements reported in this study are those of the areas that form the two-phase interface and the line that forms the TPB. These interfaces are of importance to the function and performance of the structure for systems like the SOFC anode. These interfaces perform a number of important operations. For example, if a hydrocarbon fuel such as methane is being used, the Ni surface can behave as a catalyst and can help to breakdown to the fuel to hydrogen and corresponding by-products. The hydrogen is often considered a simpler molecule to directly electrochemically oxidize. For this scenario, the pore–Ni area can be of considerable importance. Further, if the Ni coarsens or agglomerates over time, the catalytic area available to perform such operations can be reduced. Similar scenarios can be posed for the Ni–YSZ interface within the anode, which forms the electrochemical double layer. One of the most cited interfaces in the SOFC community is the TPB line that forms at the union of the Ni, YSZ, and pore phases. This boundary is where the electrochemical oxidation occurs and is directly related to the structure's electrochemical activity. Understanding this interface, and how it may change with operation, can provide considerable insight to the community.

Because of the importance of the interfaces within the heterogeneous SOFC electrode structure, an additional aspect is considered. The areas and lines that these interfaces form are of considerable importance; however, not all of them may be active due to non-contiguous regions. On the basis of the processes these interfaces support, and that transport processes support this interfacial phenomenon, the amount of *active* interfaces may be a better measure of the heterogeneous structure. Specifically, if the interface that supports a given process cannot be reached by the participating species, the interface does not play a functional role. These effects can be treated by examining the interface measurements both with and without the non-contiguous regions of the phases participating in the respective interface.

Verification of the interface measurement algorithms has been completed using numerous simplified, yet unique phenomenological structures. These structures were generated by the authors and made in such a way that the TPB length and phase-interface areas were known *a priori*. All of the structures were also mirrored along the primary planes to ensure all directional routines are functioning properly.

With confidence in the interface algorithms, the two-phase area and TPB lengths are examined. This effort considers the three structures generated for this study, with interface measurements for the XCT sample already reported [1]. In Table 4, the contiguous and absolute interfacial areas and TPB length are provided for the full 5^3 μm^3 volumes. The ratio of these measurements is also provided.

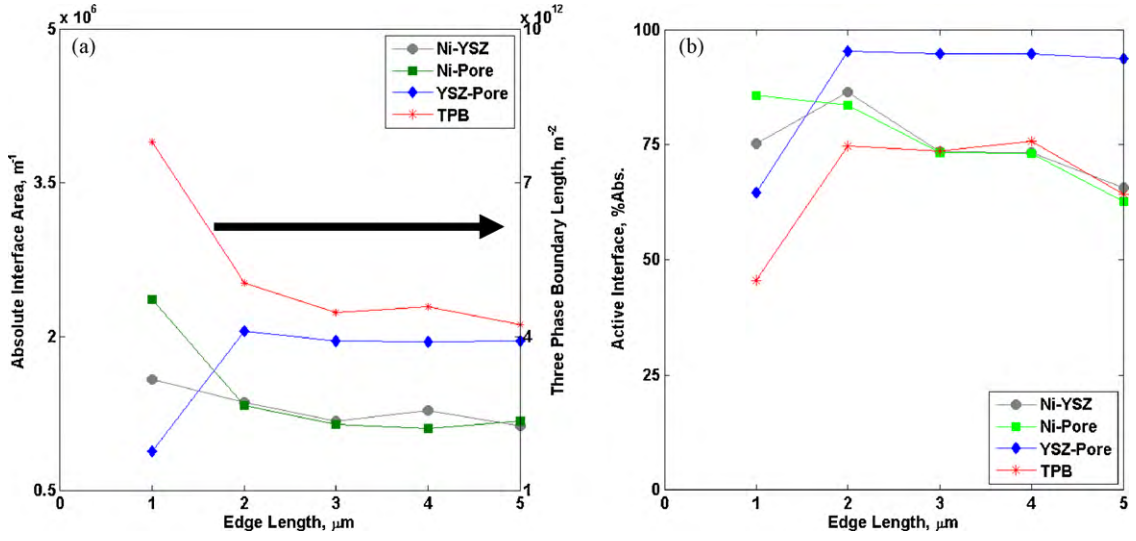

Fig. 10. The absolute two- and three-phase interfaces for the sphere-packing structure are shown as a function of the edge length of the cubic volume. The (a) absolute two-phase interfacial areas and three-phase boundary lengths, as well as the (b) percentage of the absolute two- and three-phase interfaces that is contiguous.

Table 4
Volume specific phenomenological structure interfacial measurements.

Interface	Contiguous	Absolute	Ratio
Ni–YSZ	0.74×10^6, m^{-1}	1.13×10^6, m^{-1}	0.66
YSZ–pore	1.84×10^6, m^{-1}	1.96×10^6, m^{-1}	0.94
Ni–pore	0.74×10^6, m^{-1}	1.17×10^6, m^{-1}	0.63
Ni–YSZ–pore	2.72×10^{12}, m^{-2}	4.24×10^{12}, m^{-2}	0.64

In Table 4, a substantial difference between the absolute and contiguous interfaces is recognized. Further, it is recognized that the interfaces involving the Ni regions, which was previously noted for maintaining large non-contiguous regions in this study, have a substantially reduced amount of active interfaces.

As is reflected in Table 4, the volumetric independence study is presented in Fig. 10(a) for the absolute interfacial measurements for the sphere-packing generated samples. Meanwhile, Fig. 10(b) provides the volumetric interdependence for percentage of active interfaces in these same samples. In Fig. 10(a), it appears as if volumetric independence starts to develop for all of the interface measurements for volumes of 3^3 μm^3. In examining the volumetric independence for the percentage of active interfaces within these same samples in Fig. 10(b), similar effects to those noted in the contiguity measurements are recognized. This similarity occurs because an individual phase with reduced contiguity relative to the others is more likely to dominate the magnitude of the active interfaces. In the context of the sphere-packing sample, these effects are rather quite lucid. However, it is preliminary to suggest an underlying trend. The lack of contiguity in the Ni regions of the sphere-packing sample was a surprise to the authors. Therefore, additional consideration will need to be given to these types of measurements in actual samples in the near future.

5. Conclusions

A detailed description of characterization and analysis methods that have been developed, adapted, and used by the authors in several recent studies have been presented [1,2,25]. Specific methods discussed in this work are those that the authors have used to examine the volume fractions, volumetric contiguity, tortuosity, and two- and three-phase interfaces for the examination of the heterogeneous SOFC electrode structures. In a second part of this work, more detailed quantitative characterizations related to the contributions of different transport cross-sectional diameters and their effect on transport-related losses are considered [3].

Among the more interesting observations made in the present study are the unique volumetric dependencies for the measurements made on the pore regions of the imaged samples; whether it is the volume fraction, tortuosity, and/or contiguity. Further, unique methods used to independently measure the tortuosity of these regions were shown. Samples that were artificially generated using sphere-packing routines were used to demonstrate the volumetric dependence of the two- and three-phase boundaries. The absolute measurements as well as the measurement of the interfaces that maintain contiguous pathways through the sample structure were made. In this specific study, large non-contiguous regions of the Ni-phase in the sphere-packing generated structure were observed and had a substantial impact on the modified interface measurements involving this phase. This effect is attributed to the artificial methods used to digitally generate this structure and therefore should only be considered as phenomenological. However, these measurements and methods can have a future impact on how well the sample structure is used in terms of supporting the necessary transport and reaction processes. Further, it can have a direct impact on the measurement of degradation of the electrode structures in terms of both manufacturing and operational conditions in future studies.

Acknowledgments

The authors gratefully acknowledge financial support from the Army Research Office Young Investigator Program (Award 46964-CH-YIP), the National Science Foundation (Award CBET-0828612), an Energy Frontier Research Center on Science Based Nano-Structure Design and Synthesis of Heterogeneous Functional Materials for Energy Systems funded by the U.S. Department of Energy, Office of Science, Office of Basic Energy Sciences (Award DE-SC0001061) and the ASEE National Defense Science and Engineering Graduate Fellowship program. The authors also acknowledge the use of the Advanced Photon Source supported by the U.S. Department of Energy, Office of Science, Office of Basic Energy Sciences, under Contract No. DE-AC02-06CH11357. The authors would like to thank Adaptive Materials Inc., for the SOFC samples, Dr. Yong S. Chu (Brookhaven National Laboratory) for discussions and assistance with the collection of the elemental phase imaged XCT data, Prof. George J. Nelson (University of Connecticut) for proofreading the manuscript, and Brandon Chalifoux for the development of Fig. 6.

References

[1] K.N. Grew, Y.S. Chu, Y. Jaemock, A.A. Peracchio, J.R. Izzo Jr., Y. Hwu, F. De Carlo, W.K.S. Chiu, J. Electrochem. Soc. 157 (6) (2010) B783–B792.
[2] J.R. Izzo Jr., A.S. Joshi, K.N. Grew, W.K.S. Chiu, A. Tkachuk, S.H. Wang, W. Yun, J. Electrochem. Soc. 155 (5) (2008) B504–B508.
[3] K.N. Grew, A.A. Peracchio, W.K.S. Chiu, J. Power Source, 2010, doi:10.1016/j.jpowsour.2010.07.006, in press.
[4] J.B. Goodenough, H.D. Abruna, M.V. Buchana, S. Visco, M. Stanley, B. Dunn, Y. Gogotsi, A. Gewirth, D. Nocera, Basic Research Needs for Electrical Energy Storage: Report of the Basic Energy Sciences Workshop on Electrical Energy Storage, U.S. Department of Energy, 2007.
[5] A.T. Bell, B.C. Gates, D. Ray, M. Barteau, D.G. Nocera, D.G. Johnson, M.L. Johnson Jr., H.W. Blanch, G.W. Huber, M. Henderson, P.C. Stair, J. Chen, B. Garrett, V.S.Y. Lin, T.D. Tilley, Basic Research Needs: Catalysis for Energy, U.S. Department of Energy, 2007.
[6] W. Eberhardt, F. Himpsel, N. Berrah, G. Brown, H. Durr, R. Hemley, J.C. Hemminger, J. Kirz, R. Osgood, J. Phillips, R. Schlogl, Z.X. Shen, Next Generation Photon Sources for Grand Challenges in Science and Energy: A Report to a Subcommittee to the Basic Energy Sciences Advisory Committee, U.S. Department of Energy, 2009.
[7] J. Wadsworth, G.W. Crabtree, R.J. Hemley, M. Buchanan, R. Falcone, I. Robertson, J. Stringer, P. Tortorelli, G.T. Gray, M. Nicol, J. Lehr, S.W. Tozer, T.D. de la Rubia, Basic Research Needs for Materials Under Extreme Environments: Report of the Basic Energy Sciences Workshop on Materials Under Extreme Environments, U.S. Department of Energy, 2007.
[8] T.L. Reitz, H. Xiao, M. Rottmayer, T. Seibert, ECS Trans. 7 (1) (2007) 687–696.
[9] H. Tu, U. Stimming, J. Power Source 127 (1–2) (2004) 284–293.
[10] H. Yokokawa, H. Tu, B. Iwanschitz, A. Mai, J. Power Source 182 (2) (2008) 400–412.
[11] P. Tanasini, M. Cannarozzo, P. Costamagna, A. Faes, J. Van Herle, A. Hessler-Wyser, C. Comninellis, Fuel Cell 9 (5) (2009) 740–752.
[12] A. Faes, A. Nakajo, A. Hessler-Wyser, D. Dubois, A. Brisse, S. Modena, J. Van Herle, J. Power Source 193 (1) (2009) 55–64.
[13] M. Pihlatie, A. Kaiser, P.H. Larsen, M. Mogensen, J. Electrochem. Soc. 156 (3) (2009) B322–B329.
[14] T. Klemensø, C.C. Appel, M. Mogensen, Electrochem. Solid State Lett. 9 (9) (2006) A403–A407.
[15] T. Klemensø, C. Chung, P.H. Larsen, M. Mogensen, J. Electrochem. Soc. 152 (11) (2005) A2186–A2192.
[16] A. Atkinson, S. Barnett, R.J. Gorte, J.T.S. Irvine, A.J. McEvoy, M. Mogensen, S.C. Singhal, J. Vohs, Nat. Mater. 3 (1) (2004) 17–27.
[17] R. Clague, P. Aguiar, D.J.L. Brett, A.J. Marquis, S. Schottl, R. Simpson, N.P. Brandon, ECS Trans. 5 (1) (2007) 521–532.
[18] G. Ju, K. Reifsnider, X. Huang, ASME J. Fuel Cell Sci. Technol. 5 (3) (2008) 031006.
[19] M. Pillai, Y. Lin, H. Zhu, R.J. Kee, S.A. Barnett, J. Power Source 195 (1) (2010) 271–279.
[20] M.D. Gross, J.M. Vohs, R.J. Gorte, J. Mater. Chem. 17 (30) (2007) 3071–3077.
[21] H. He, J.M. Vohs, R.J. Gorte, J. Power Source 144 (1) (2005) 135–140.
[22] M.B. Pomfret, J. Marda, G.S. Jackson, B.W. Eichhorn, A.M. Dean, R.A. Walker, J. Phys. Chem. C 112 (13) (2008) 5232–5240.
[23] A. Hauch, J.R. Bowen, L.T. Kuhn, M. Mogensen, Electrochem. Solid State Lett. 11 (3) (2008) B38–B41.

[24] K.N. Grew, A.A. Peracchio, J.R. Izzo Jr., W.K.S. Chiu, ECS Trans. 25 (2) (2009) 1861–1870.
[25] A.S. Joshi, K.N. Grew, J.R. Izzo Jr., A.A. Peracchio, W.K.S. Chiu, ASME J. Fuel Cell Sci. Technol. 7 (1) (2010) 011006.
[26] J.R. Wilson, W. Kobsiriphat, R. Mendoza, H.-Y. Chen, J.M. Hiller, D.J. Miller, K. Thornton, P.W. Voorhees, S.B. Adler, S.A. Barnett, Nat. Mater. 5 (7) (2006) 541–544.
[27] J.R. Wilson, S.A. Barnett, Electrochem. Solid State Lett. 11 (10) (2008) B181–B185.
[28] D. Gostovic, J.R. Smith, D.P. Kundinger, K.S. Jones, E.D. Wachsman, Electrochem. Solid State Lett. 10 (12) (2007) B214–B217.
[29] A. Tkachuk, F. Duewer, H. Cui, M. Feser, S. Wang, W. Yun, Z. Kristallogr. 222 (11) (2007) 650–655.
[30] M. Feser, J. Gelb, H. Chang, H. Cui, F. Duewer, S.H. Lau, A. Tkachuk, W. Yun, Meas. Sci. Technol. 19 (9) (2008) 094001.
[31] F. Natterer, The Mathematics of Computerized Tomography, Wiley, New York, 1986.
[32] X. Zeng, F. Duewer, M. Feser, C. Huang, A. Lyon, A. Tkachuk, W. Yun, Appl. Opt. 47 (13) (2008) 2376–2381.
[33] Y.-T. Chen, T.-N. Lo, Y.S. Chu, J. Yi, C.-J. Liu, J.-Y. Wang, C.-L. Wang, C.-W. Chiu, T.-E. Hua, Y. Hwu, Q. Shen, G.-C. Yin, K.S. Liang, H.-M. Lin, J.H. Je, G. Margaritondo, Nanotechnology 19 (39) (2008) 395302.
[34] Y.S. Chu, J.M. Yi, F. De Carlo, Q. Shen, W.-K. Lee, H.J. Wu, C.L. Wang, J.Y. Wang, C.J. Liu, C.H. Wang, S.R. Wu, C.C. Chien, Y. Hwu, A. Tkachuk, W. Yun, M. Feser, K.S. Liang, C.S. Yang, J.H. Je, G. Margaritondo, Appl. Phys. Lett. 92 (10) (2008) 103119.
[35] S. Sunde, J. Electrochem. Soc. 143 (6) (1996) 1930–1939.
[36] S. Sunde, J. Electrochem. Soc. 143 (3) (1996) 1123–1132.
[37] S. Sunde, Electrochim. Acta 42 (17) (1997) 2637–2648.
[38] S. Sunde, J. Electroceram. 5 (2) (2000) 153–182.
[39] W.G. Bessler, S. Gewies, M. Vogler, Electrochim. Acta 53 (4) (2007) 1782–1800.
[40] M. Cannarozzo, A.D. Borghi, P. Costamagna, J. Appl. Electrochem. 38 (7) (2008) 1011–1018.
[41] M. Cannarozzo, S. Grosso, G. Agnew, A. Del Borghi, P. Costamagna, ASME J. Fuel Cell Sci. Technol. 4 (1) (2007) 99–106.
[42] P. Costamagna, P. Costa, V. Antonucci, Electrochim. Acta 43 (3–4) (1998) 375–394.
[43] P. Costamagna, P. Costa, E. Arato, Electrochim. Acta 43 (8) (1997) 967–972.
[44] S. Torquato, Ann. Rev. Mater. Sci. 32 (2002) 77–111.
[45] S. Hyun, S. Torquato, J. Mater. Res. 16 (1) (2001) 280–285.
[46] S. Torquato, S. Hyun, A. Donev, J. Appl. Phys. 94 (9) (2003) 5748–5755.
[47] J.R. Izzo Jr., A.A. Peracchio, W.K.S. Chiu, J. Power Source 176 (1) (2008) 200–206.
[48] E.W. Washburn, Phys. Rev. 17 (1921) 273–283.
[49] M.M. Denn, Process Fluid Mechanics, Prentice-Hall, Englewood Cliffs, NJ, 1980.
[50] N. Epstein, Chem. Eng. Sci. 44 (3) (1989) 777–779.
[51] S.C. DeCaluwe, H. Zhu, R.J. Kee, G.S. Jackson, J. Electrochem. Soc. 155 (6) (2008) B538–B546.
[52] V.H. Schmidt, C.-L. Tsai, J. Power Source 180 (1) (2008) 253–264.
[53] P. Grathwohl, Diffusion in Natural Porous Media: Contaminant Transport, Sorption/Desorption and Dissolution Kinetics, Kluwer Academic Publishers, Boston, 1998.